AD_____

Award Number: DAMD17-02-1-0081

TITLE: Compact Positron Tomograph for Prostate Imaging

PRINCIPAL INVESTIGATOR: Jennifer S. Huber, Ph.D.

CONTRACTING ORGANIZATION: Ernest Orlando Lawrence Berkeley
National Laboratory
Berkeley, CA 94701

REPORT DATE: January 2004

TYPE OF REPORT: Annual

PREPARED FOR: U.S. Army Medical Research and Materiel Command
Fort Detrick, Maryland 21702-5012

DISTRIBUTION STATEMENT: Approved for Public Release;
Distribution Unlimited

The views, opinions and/or findings contained in this report are those of the author(s) and should not be construed as an official Department of the Army position, policy or decision unless so designated by other documentation.

REPORT DOCUMENTATION PAGE

Form Approved
OMB No. 074-0188

1. AGENCY USE ONLY (Leave blank)	2. REPORT DATE	3. REPORT TYPE AND DATES COVERED
	January 2004	Annual (10 Dec 2002 - 9 Dec 2003)

4. TITLE AND SUBTITLE

Compact Positron Tomograph for Prostate Imaging

5. FUNDING NUMBERS

DAMD17-02-1-0081

6. AUTHOR(S)

Jennifer S. Huber, Ph.D.

7. PERFORMING ORGANIZATION NAME(S) AND ADDRESS(ES)

Ernest Orlando Lawrence Berkeley
National Laboratory
Berkeley, CA 94701

E-Mail:

8. PERFORMING ORGANIZATION REPORT NUMBER

9. SPONSORING / MONITORING AGENCY NAME(S) AND ADDRESS(ES)

U.S. Army Medical Research and Materiel Command
Fort Detrick, Maryland 21702-5012

10. SPONSORING / MONITORING AGENCY REPORT NUMBER

11. SUPPLEMENTARY NOTES

Original contains color plates: ALL DTIC reproductions will be in black and white

12a. DISTRIBUTION / AVAILABILITY STATEMENT

Approved for Public Release; Distribution Unlimited

12b. DISTRIBUTION CODE

13. ABSTRACT (Maximum 200 Words)

The goal of this project is to construct a functioning compact positron tomograph, whose geometry is optimized for detecting prostate tumors with molecular tracers such as [^{11}C]choline (carbon-11 choline), in order to confirm the presence, absence or progression of prostate cancer. When completed, the camera will consist of two banks of detectors mounted in a gantry. The bottom bank is fixed below the patient bed, and the top bank moves upward for patient access and downward for maximum sensitivity.

During the first 22 months of funding, we have optimized and completed the tomograph design, fabricated all gantry components and nearly completed construction of the gantry and electronics housing, acquired and tested all detector modules and electronics, developed an iterative reconstruction algorithm for the special camera geometry, and simulated the reconstruction of realistic Monte Carlo data. Progress is on schedule.

14. SUBJECT TERMS	15. NUMBER OF PAGES
Positron emission tomography, prostate	24
	16. PRICE CODE

17. SECURITY CLASSIFICATION OF REPORT	18. SECURITY CLASSIFICATION OF THIS PAGE	19. SECURITY CLASSIFICATION OF ABSTRACT	20. LIMITATION OF ABSTRACT
Unclassified	Unclassified	Unclassified	Unlimited

3. TABLE OF CONTENTS

1. Cover 1
2. SF 298 2
3. Table of Contents 3
4. Introduction 4
5. Body 4
6. Key Research Accomplishments 8
7. Reportable Outcomes 8
8. Conclusions 8
9. References 8
10. Appendices 9

4. INTRODUCTION

The goal of this project is to construct a functioning compact positron tomograph, whose geometry is optimized for detecting prostate tumors with molecular tracers such as [^{11}C]choline (carbon-11 choline), to confirm the presence, absence or progression of prostate cancer. Compared with a conventional positron emission tomography (PET) camera, the proposed tomograph has (1) the same spatial resolution in the region of the prostate; (2) improved detection efficiency; and (3) significantly lower cost, which would increase clinical availability. See Figure 1 for a sketch of the positron tomograph, consisting of detector banks, patient and patient bed. See Figure 2 for photographs of a detector module and partially-assembled camera. See Appendix 1 for 3-D drawings of the positron tomograph with some gantry details. See Appendices 2 and 3 for technical papers presented at scientific meetings.

5. BODY OF THE PROGRESS REPORT

Below are the list of tasks as proposed in our original Statement of Work. A summary of our progress and current status for each sub-task follows.

Task 1 Design two external curved detector banks; Months 1-10:

a) Determine optimal detector bank geometry based on simulations and calculations.
b) Design shielding.
c) Design gantry.
d) Design phantom bed.

Task 2 Construct the camera; Months 3-26:

a) Construct gantry.
b) Purchase and test CTI ECAT HR+ PET detector modules.
c) Configure detector modules into two detector banks.
d) Construct and test event processing, coincidence processing, and readout electronics.
e) Configure system with phantom bed.

Task 3 Develop iterative reconstruction algorithms; Months 2-31:

a) Develop iterative algorithms using Monte Carlo generated data.
b) Optimize algorithms using real data.

Task 4 Characterize camera performance with phantoms; Months 27-36.

Task 1(a): Determine optimal detector bank geometry

Based on our computer simulations and calculations, we have optimized and finalized the design of the PET camera [1, 2]. Figure 1 shows the transaxial and sagittal views of the camera. The bottom bank is fixed below the patient bed, and the top bank moves upward for patient access and downward for maximum sensitivity. Each bank consists of two axial rows of 20 CTI ECAT HR+ detector modules, forming two arcs with a minor axis of 45 cm and a major axis of 70 cm. Our original proposal allowed for only a single axial row, but patient alignment will be easier with greater axial coverage; we negotiated with CPS Innovations to receive the CTI ECAT HR+ detector modules at below cost (to

afford the 2nd axial row). Individual detector modules are angled to point towards the camera center in order to optimize resolution at the center near the prostate at the price of some resolution degradation at the edges. Both detector banks can be tilted to image the prostate while minimizing attenuation (*i.e.*, above the buttocks and below the stomach, see Figure 1), but the gantry allows zero tilt for thin patients.

Task 1(b): Design shielding

The camera design includes shielding (see Figure 1b). Inter-plane tungsten septa extend beyond the scintillator crystals to reduce background events from random coincidences and from photons that Compton scatter in the patient. Lead shields are also used on the ends to reduce activity from outside the field of view. Our original septa design consisted of septa with an uniform length of 5 cm, based on geometric calculations with reference to current clinical whole-body scanners. However, we have recently used Monte Carlo simulations to further investigate several novel septa designs, in addition to considering manufacturing techniques. We now have two improved septa designs [3] with septa that vary in length depending on the arc position. The first design places septa (0.8 mm thick, with a length that varies from 2 cm at the minor axis to 5 cm at the major axis) axially between each scintillator crystal. The second design places septa (2.4 mm thick, with a length that varies from 10 cm to 20 cm) axially between detector blocks. We'll choose between these two novel designs shortly, based on cost and expected performance.

Task 1(c): Design gantry

The gantry and electronics housing is designed. Appendix 1 shows 3-D drawings of the camera with many of the gantry and electronics housing details. The upper bank is mounted on a main aluminum back-plate in order to control the vertical motion using a hand-crank, allowing upward movement for patient access and downward to maximize sensitivity. A second hand-crank is used to adjust the overall tilt of both upper and lower banks. The near end of Appendix 1(a) also shows the electronics housing; see Appendix 2 for further electronics details. The electronics used for another project is similar to this system [4]. The ±5V and high-voltage power supplies are visible in Appendix 1b.

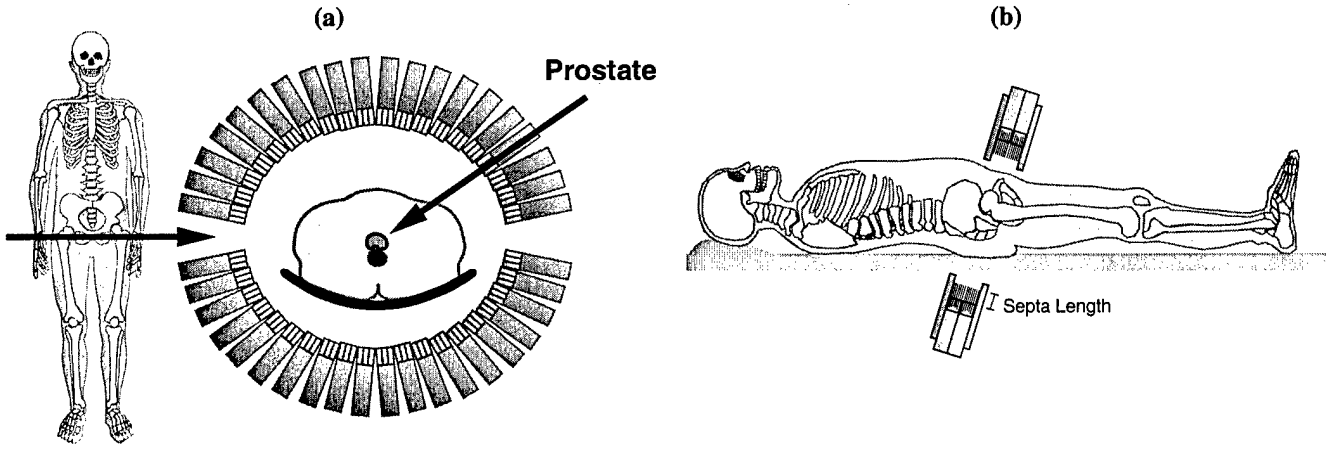

Figure 1: Positron tomograph for prostate imaging. (a) Drawing of a transaxial view through prostate, showing the patient centered between two detector banks (shielding not shown). The individual detector modules are angled to point towards the prostate. (b) Drawing of the sagittal view with shielding shown. The bottom arc is fixed below the patient bed, whereas the top arc adjusts vertically for patient access and compactness. Both detector banks are tilted and positioned as close as possible to the prostate, which improves sensitivity and minimizes attenuation.

Task 1(d): Design phantom bed

Our proposal is limited to the design, construction and characterization (using phantoms) of a compact prostate imaging system. Since human studies are beyond the scope of this proposal, we have only designed a simple phantom bed at this time.

Task 2(a): Construct gantry

The gantry and electronics housing are under construction, and completion is expected before April, 2004 (*i.e.,* month 26). All gantry components have been machined or purchased, and the main gantry assembly is complete. Assembly of the electronics housing, cabling, and power supplies is in progress. Figure 2b shows a photograph of the partially-assembled camera, taken before the lead shielding was glued in place.

Task 2(b): Purchase and test CTI ECAT HR+ PET detector modules

We have acquired all CTI ECAT HR+ detector modules and electronics boards from CPS Innovations at a reduced cost. All detector modules have been tested and demonstrated to work properly.

Task 2(c): Configure detector modules into two detector banks

Figure 2 shows photographs of a detector module and partially-assembled camera. All 80 detector modules will be configured into two detector banks as soon as the gantry and electronics housing assembly is complete.

Task 2(d): Construct and test event processing, coincidence processing, and readout electronics

We have tested and modified the CPS Innovations electronics and data acquisition software for our system, as well as designed and constructed the required conversion boards (for the Analog Subsection boards). We have tested the event processing, coincidence processing and readout electronics using test pulses. We are currently modifying software (e.g., software to calibrate the detector modules).

Task 2(e): Configure system with phantom bed

We have not yet begun this task. We expect to configure the system with the phantom bed this year.

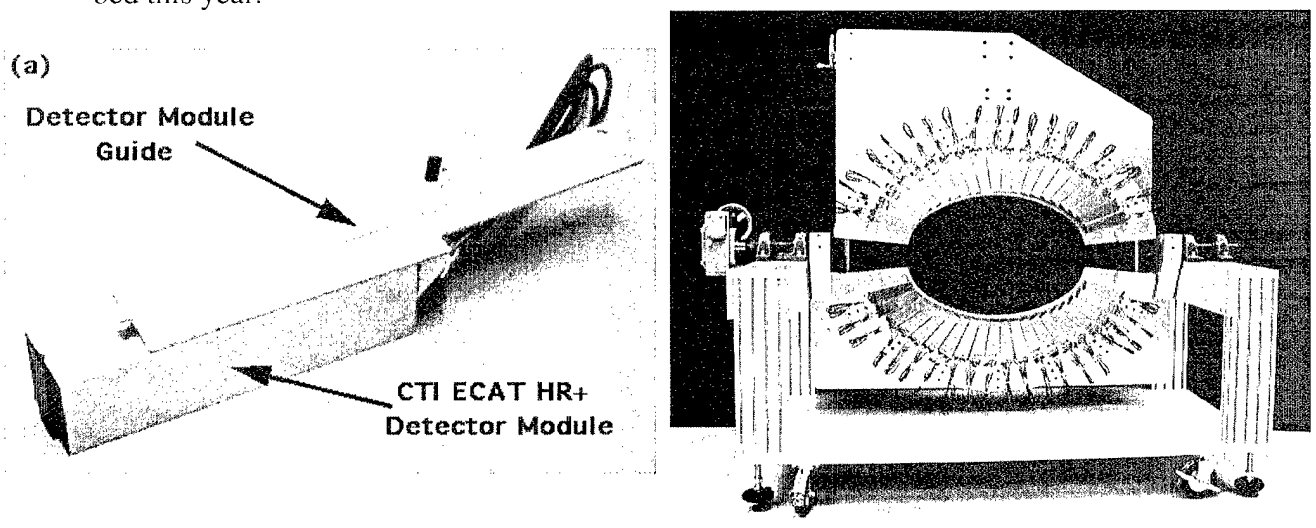

Figure 2: (a) CTI ECAT HR+ detector module with an aluminum guide epoxied along its midline. (b) Photograph of the partially-assembled camera with a single axial row of detector modules. Each detector module has an aluminum guide that slides along a groove in the arc plate and is stopped (and secured against the arc plate) using a mortise and tenon. The detector modules are individually angled to point towards the center of the camera.

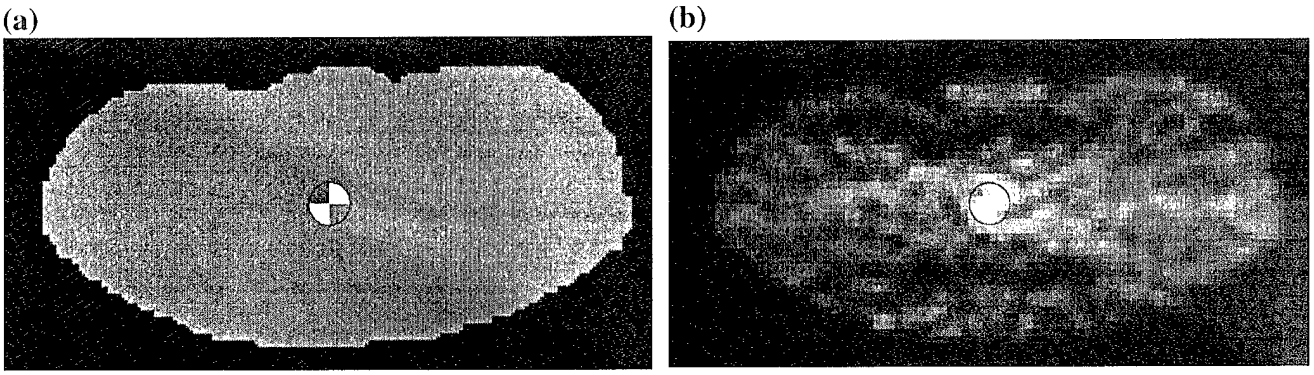

Figure 3: (a) Body outline of patient with 2.5 cm diameter circular "prostate" divided into quadrants with "tumors" placed in the upper right and lower left quadrants (white = high uptake), assuming a tumor to background ratio of 2:1. The "patient" is 37.5 cm wide and 18.0 cm deep. (b) Reconstructed image of the phantom using an iterative maximum likelihood algorithm that assumes a 30% scatter fraction and 20% randoms fraction. The image represents 745 kcounts in a single slice, which should be achievable with a 6-minute scan after a 10 mCi injection. Both tumors are clearly visible.

Task 3(a): Develop iterative algorithms using Monte Carlo generated data

The reconstruction algorithm is under development. We have done a significant amount of simulation work to evaluate the expected camera performance as well as to optimize the camera design. We have determined the size of the region with high spatial resolution within our PET camera, showing that there will be good resolution in the 10 cm diameter central region near the prostate for a wide range of patient sizes [2]. We have addressed the issue of irregular and incomplete sampling due to the side gaps between the detector banks [1].

Monte Carlo methods have been used to study the reconstruction of extended prostate sources. Reconstructions were performed with an iterative maximum likelihood technique that assumes statistical noise representing 745 kcounts/slice, a tumor activity concentration that is two times the background activity concentration, 30% scatter fraction, and 20% randoms fraction. The reconstructions were then post-filtered with a very conservative Gaussian function of sigma = 1 pixel = 2 mm. We have demonstrated that we can reconstruct nearly artifact-free images, as well as detect and differentiate partial and whole prostate tumors, using Monte Carlo data equivalent to a 6-minute scan after a 10 mCi radiopharmaceutical injection (see Figure 3). The expected camera performance is discussed in further detail in Appendix 2. We have explored the necessary data corrections, such as attenuation correction and normalization. Further development is still needed, including the incorporation of scatter and the optimization of the algorithm using Monte Carlo data.

Task 3(b): Optimize algorithms using real data

We have not yet begun this task. We expect to optimize the algorithm using real data this year.

Task 4: Characterize camera performance with phantoms

We have not yet begun this task. Characterization of camera performance with phantoms will be described in the next progress report.

6. KEY RESEARCH ACCOMPLISHMENTS

- The camera design was optimized and completed.
- All gantry components were fabricated, and the main gantry assembly was completed.
- Designs for electronics, packaging, mounting and interconnects were completed. Construction will be completed before April, 2004.
- All detector modules and electronics were acquired and tested.
- Extensive simulations were used to evaluate the expected camera performance.

7. REPORTABLE OUTCOMES

J. S. Huber, J. Qi, S. E. Derenzo, et al., "The Development of a Compact Positron Tomograph for Prostate Imaging," *LBNL-50790*, 2002. Oral presentation at the 2002 IEEE Medical Imaging Conference.

J. Qi, J. S. Huber, R.H. Huesman, W. W. Moses, S. E. Derenzo, and T. F. Budinger, "Septa Design for a Prostate-Specific PET Camera," *IEEE Trans Nucl Sci*, Submitted, 2003. Oral presentation at the 2003 IEEE Medical Imaging Conference.

8. CONCLUSIONS

Task 1 has been completed. Design of the detector bank geometry, electronics, gantry, electronics housing and patient bed was optimized and completed. Septa design was improved.

Task 2 is in progress and on schedule. The gantry components were fabricated, and the main gantry assembly was completed. All detector modules and electronics were acquired and tested. DAQ software was modified, and further software development is in progress. A phantom bed was constructed. The system will be configured once the gantry and electronics housing assembly is complete. No problems related to this task are currently anticipated.

Task 3 is in progress and on schedule. Extensive simulations were used to evaluate the expected camera performance, demonstrating that our PET camera design will image prostate tumors with good spatial resolution and image contrast at low cost relative to commercial PET scanners, in agreement with our original proposal. A preliminary iterative reconstruction algorithm was developed, but further development is necessary.

Task 4 has not yet begun.

9. REFERENCES

[1] J. S. Huber, S. E. Derenzo, J. Qi, et al., "Conceptual Design of a Compact Positron Tomograph for Prostate Imaging," *IEEE Trans Nucl Sci*, vol. NS-48, pp. 1506-1511, 2001.

[2] J. S. Huber, J. Qi, S. E. Derenzo, et al., "The Development of a Compact Positron Tomograph for Prostate Imaging," *LBNL-50790*, 2002.

[3] J. Qi, J. S. Huber, R. H. Huesman, et al., "Septa Design for a Prostate-Specific PET Camera," *IEEE Trans Nucl Sci*, Submitted, 2003.

[4] W. W. Moses, J. W. Young, K. Baker, et al., "The Electronics System for the LBNL Positron Emission Mammography (PEM) Camera," *IEEE Trans Nucl Sci*, vol. NS-48, pp. 632-636, 2001.

10. APPENDICES

Appendix 1: 3-D color drawings of the PET camera with some gantry details; (a) as viewed from the electronics end and (b) as viewed from the power supply/doctor access end.

Appendix 2: J. S. Huber, J. Qi, S. E. Derenzo, et al., "The Development of a Compact Positron Tomograph for Prostate Imaging," *LBNL-50790*, 2002.

Appendix 3: Preprint of J. Qi, J. S. Huber, R. H. Huesman, et al., "Septa Design for a Prostate-Specific PET Camera," *IEEE Trans Nucl Sci*, Submitted, 2003.

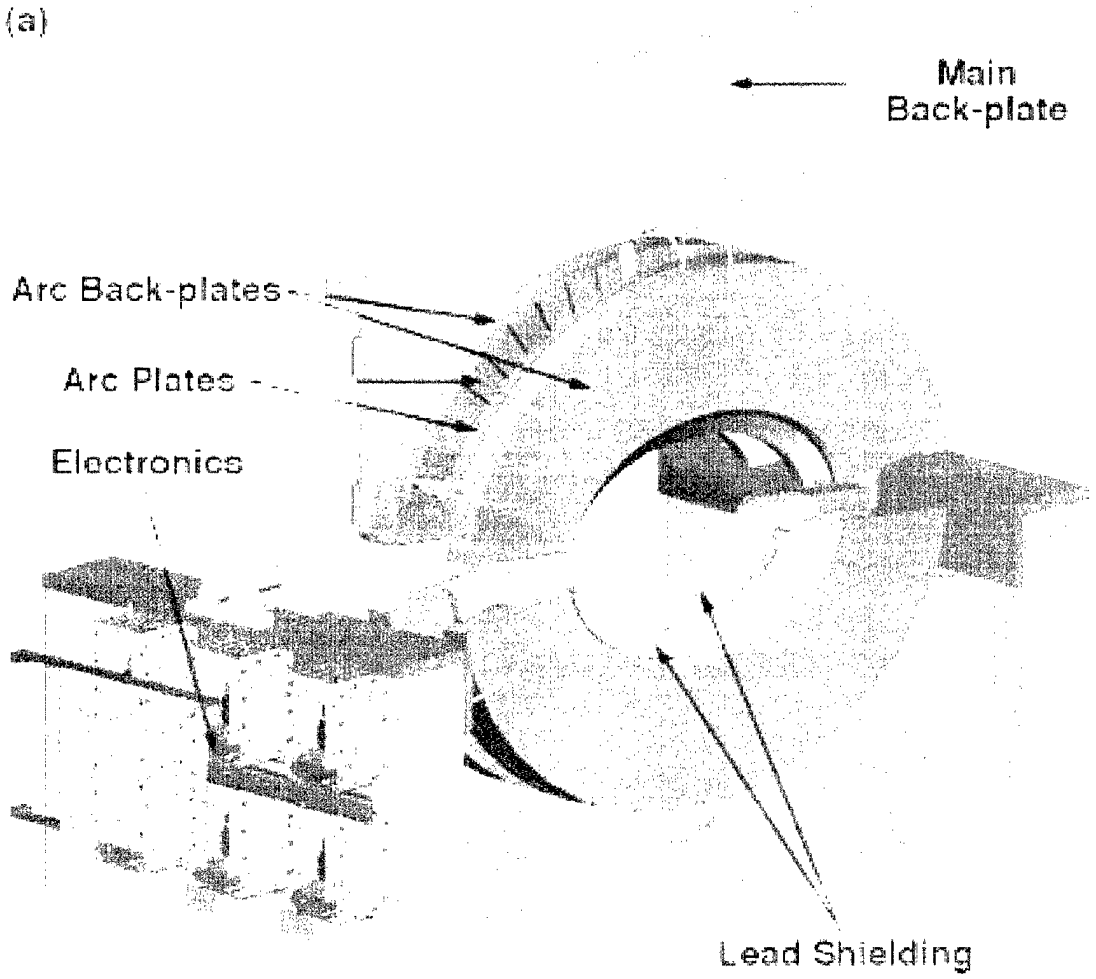

Appendix 1: 3-D color drawings of the prostate PET camera with some gantry details. Only a few detector modules are shown in place. The arc plates are mounted on thicker aluminum arc back-plates that also hold the lead shielding in place. The arc plates (pink), arc back-plates (blue) and lead shielding (green) are symmetrical since there are two axial rows of detector modules. The upper bank is mounted on a main aluminum back-plate in order to control the vertical motion using a hand-crank, allowing upward movement for patient access and downward to maximize sensitivity. A second hand-crank is used to adjust the overall tilt of both upper and lower banks. Most of the cabling is not shown, as well as the patient bed. (a) The near end of the drawing shows the electronics. The six Detector Head Interface boards are mounted horizontally to the housings that hold their corresponding Analog Subsection boards. The Coincidence Processor board is mounted on the cabinet door. (b) The near end of the drawing shows the power supplies.

(b)

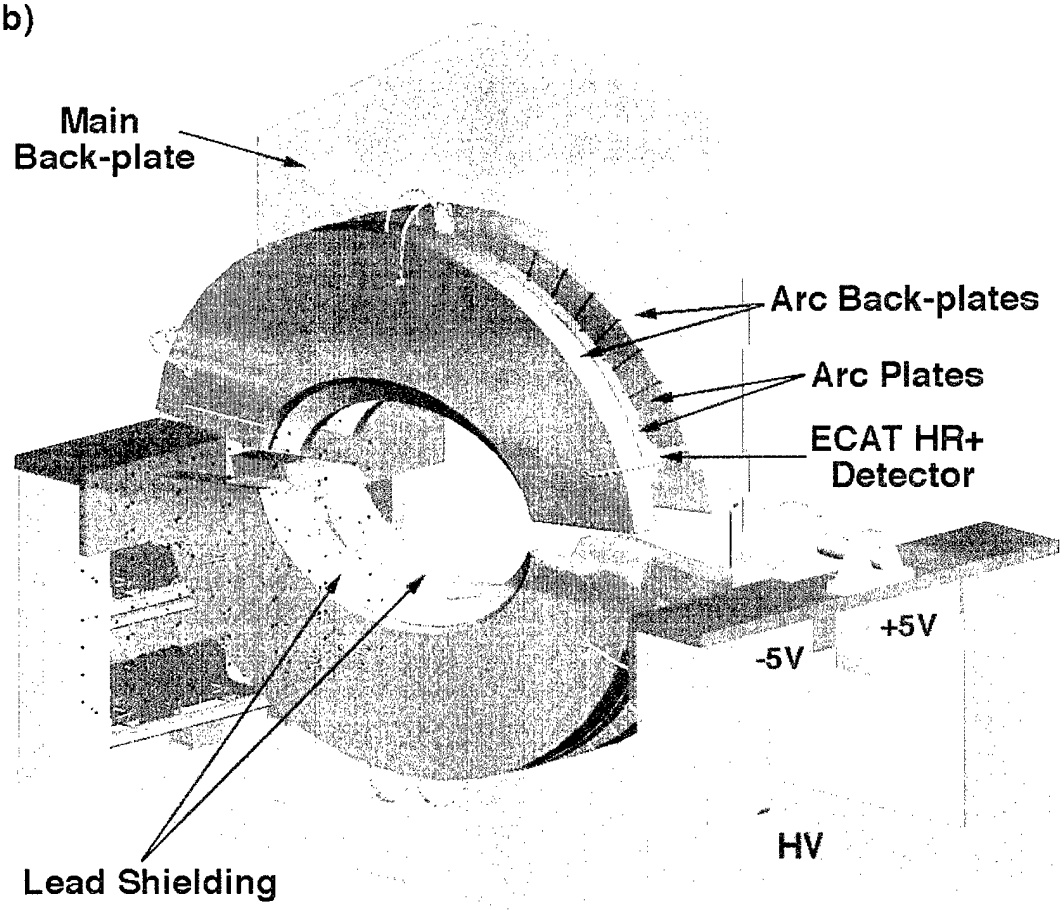

The Development of a Compact Positron Tomograph for Prostate Imaging

J. S. Huber, *Member, IEEE,* J. Qi, *Member, IEEE,* S. E. Derenzo, *Fellow, IEEE,* W. W. Moses, *Senior Member, IEEE,* R. H. Huesman, *Fellow, IEEE,* and T. F. Budinger, *Member, IEEE*

Abstract—We give design details and expected image results of a compact positron tomograph designed for prostate imaging that centers a patient between a pair of external curved detector banks (ellipse: 45 cm minor, 70 cm major axis). The bottom bank is fixed below the patient bed, and the top bank moves upward for patient access and downward for maximum sensitivity. Each bank is composed of two rows (axially) of 20 CTI PET Systems HR+ block detectors, forming two arcs that can be tilted to minimize attenuation. Compared to a conventional PET system, our camera uses about one-quarter the number of detectors and has almost two times higher solid angle coverage for a central point source, because the detectors are close to the patient. The detectors are read out by modified CTI HRRT data acquisition electronics. The individual detectors are angled in the plane to point towards the prostate to minimize resolution degradation in that region. Inter-plane septa extend 5 cm beyond the scintillator crystals to reduce random and scatter backgrounds. Average- to large-size patients will not be fully encircled by detector rings, causing incomplete sampling due to the side gaps. Monte Carlo simulations (including 20% randoms and 30% scatter fractions) demonstrate the feasibility of detecting and differentiating prostate tumors with a tumor to background ratio of 2:1, using a number of counts that should be achievable with a 6 minute scan after a 10 mCi injection (*e.g.,* carbon-11 choline). Simulations also predict minimal blurring in the 10 cm diameter central region for a wide range of patient sizes.

I. Introduction

WE present the development of a compact positron tomograph optimized to image the prostate. This instrument images radiopharmaceuticals that specifically localize in the prostate to confirm the presence, absence or progression of disease. It has approximately four times fewer detectors than a conventional whole-body positron emission tomograph (PET), which will reduce the cost and increase clinical availability.

Prostate cancer has a prevalence and diagnostic rate similar to breast cancer, with 360,000 new cases diagnosed each year and two million men affected by the disease in the United States. Prostate cancer suspicion is typically based on an elevated prostate-specific antigen (PSA) level or a suspicious node found during a digital rectal exam. Serum PSA values do not always correlate well with clinical diagnosis or outcomes [1-3]. Palpation is subjective, insensitive and inexact; more than half of all cancers detected today are not palpable. Treatment decision is based mainly on biopsy confirmation of prostate cancer, but the diagnostic accuracy of prostate biopsies is problematic. Typical treatment options include radical prostatectomy, external beam irradiation, brachytherapy (interstitial implantation of radioactive seeds), androgen ablation (hormone) therapy, or "watchful waiting." A major problem with prostatic cancer therapy is the question of when to treat or whether to treat at all. This is particularly problematic in the case of an increased PSA level with non-diagnostic repeated biopsies or after a prostatectomy. A new imaging technology for sensitive detection of early stage prostate cancer is needed to confirm initial diagnosis and help guide treatment decisions. In addition, a new method is needed to assess response shortly after treatment intervention.

In order to help meet these needs, we are building a compact PET camera optimized to image the prostate. Functional PET imaging will help detect malignant tumors in the prostate and/or prostate bed to confirm an elevated PSA level, as well as possibly help determine tumor "aggressiveness" based on metabolic uptake levels, in order to help guide whether to treat suspected prostatic cancer. Although not optimized to detect distant metastatic disease, this compact PET camera should also image local spread beyond the prostate bed to help guide treatment decisions such as whether a narrow or wide irradiation treatment field is needed.

Promising PET radiopharmaceuticals have recently demonstrated outstanding results in the sensitive detection of prostate cancer, inspiring a new interest in using PET for prostate cancer imaging. Consistent with the evidence of increased pool size of choline in prostate cancer [4, 5], Hara and co-workers demonstrated prostate tumor uptake by [^{11}C]choline. They find that: [^{11}C]choline clears the blood faster than FDG; its uptake in prostate tumors is significantly higher than in normal and surrounding tissues [6, 7], providing excellent tumor/normal contrast; and bladder accumulation is minimal if the correct time course is chosen [8] which is a major advantage over FDG. Additionally, they observe that [^{11}C]choline PET is more sensitive for detecting bone metastases than bone scintigraphy. Therefore,

Manuscript received December 10, 2002. This work was supported in part by the Director, Office of Science, Office of Biological and Environmental Research, Medical Science Division of the U.S. Department of Energy under Contract No. DE-AC03-76SF00098 and in part by Department of Defense grant number DAMD17-02-1-0081.

J. S. Huber, J. Qi, S. E. Derenzo, W. W. Moses, R. H. Huesman and T. F. Budinger are with the Lawrence Berkeley National Laboratory, Mailstop 55-121, 1 Cyclotron Road, Berkeley, CA 94720 USA (telephone: 510-486-6445, e-mail: jshuber@lbl.gov).

[^{11}C]choline is an attractive PET tracer for imaging primary and metastatic tumors of the prostate and potentially for other regions of the body [9-13]. Fig. 1 shows a [^{11}C]choline image of prostate cancer before and after therapy, demonstrating the ability to detect prostate carcinoma using choline and possibly its analogs. Other ^{11}C radiopharmaceuticals are also under investigation for prostate cancer PET imaging, including [^{11}C]acetate and [^{11}C]methionine.

^{18}F imaging has the advantage of a longer half-life, which increases clinical viability since an on-site cyclotron facility would not be necessary (as it would for ^{11}C imaging). Many groups have shown that PET imaging with [^{18}F]fluorodeoxyglucose (FDG) is not a good technique for prostate cancer diagnosis, because FDG is not very prostate specific (with a SUV of typically ~2) and the uptake is overcome by background primarily due to bladder accumulation. The SUV (standard uptake value) is the ratio of activity in the target tissue to the average activity in the body. However, there are several other ^{18}F radiopharmaceuticals currently under investigation for prostate cancer imaging, including [^{18}F]fluorocholine (FCH) [14, 15]. PET images using [^{18}F]fluorocholine demonstrate high standardized uptake values (*e.g.*, SUV of 8), indicating that FCH is well localized in the prostate cancer and can be imaged with good resolution if a short scan time (~five minutes) is used. Therefore, [^{18}F]fluorocholine is also an attractive PET tracer for imaging primary and metastatic tumors of the prostate.

II. Camera Design

A. Overview

These new prostate tracers have motivated us to build a low cost PET camera optimized to image the prostate. Coincidence imaging of positron emitters is achieved using a pair of external curved detector banks, one placed above and one below the patient. Fig. 2 shows the transaxial and sagittal views of the camera. The bottom bank is fixed below the patient bed, and the top bank moves upward for patient access and downward for maximum sensitivity. Each bank consists of two axial rows of 20 CTI ECAT HR+ block detectors, forming two arcs with a minor axis of 45 cm and major axis of 70 cm. Our prostate camera has about one-fourth the number of detectors as in a conventional PET system because: (a) the patient is not fully encircled in 2D, (b) an elliptical shape is used instead of a circular one, and (c) the axial coverage is only 8 cm. However, since the average distance to the detectors is approximately one-half that of a conventional 2D PET system, the solid angle for a central source is approximately double for average-sized men. Thus, we expect to achieve improved detection efficiency at a lower cost.

Individual detector modules are angled to point towards the camera center near the prostate location in order to reduce penetration effects (in the detector) for annihilation photons originating in the prostate. This increases resolution selectively in the region of the prostate and is an unique feature for a non-circular camera geometry. Annihilation photons from other parts of the field of view (FOV) will suffer increased penetration effects, but these FOV regions are less important. Both detector banks can be tilted to image the prostate while minimizing attenuation (*i.e.*, above the buttocks and below the stomach, see Fig. 2), but the gantry allows zero tilt for thin patients. A patient of average size is not fully encircled in 2D, which results in irregular and incomplete sampling due to the side gaps. Despite this incomplete sampling, we are able to reconstruct nearly artifact free images in the region of interest by using an iterative reconstruction algorithm [16].

The camera design also includes shielding [16]. Inter-plane septa extend 5 cm beyond the scintillator crystals to reduce background events from random coincidences and from photons that Compton scatter in the patient. Lead shields are also used on the ends to reduce activity from outside the field of view.

B. Electronics

Our camera uses modified commercial components in a novel geometry. We are using 80 CTI ECAT HR+ block detectors that are three attenuation lengths thick for good detection efficiency with narrow detector elements (*i.e.*, 8 x 8 arrays of 4.5 x 4.5 x 30 mm^3 BGO crystals) to achieve good spatial resolution. We are using modified front end, coincidence, and readout electronics developed by CTI for the HRRT brain imaging PET camera, as shown in Fig. 3. Since we are creating a non-standard camera with HR+ and HRRT components, a custom conversion board is necessary. Events are detected and assigned an arrival time, the crystal of interaction is identified, energy qualification is performed, and a digital word is formed using 28 CTI HRRT Analog Subsection boards. The output signals from the Analog Subsection boards are then multiplexed by six custom Detector Head Interface (DHI) boards, which are based on the CTI HRRT DHI design but each services a maximum of 15 (rather than 117) detector modules. We are using six DHI boards to allow coincidences between detector modules within the same bank and plane. A CTI Coincidence Processor identifies singles events in the different DHI boards that are in coincidence, and the output is sent to a Pentium-based computer system that accumulates the coincident data, reconstructs the images, and displays them.

We previously reported on the conceptual design of this prostate camera [16]. We have moved from the idea stage into the building stage. We have acquired all HR+ detector blocks and electronics boards. We are currently testing the CTI electronics and modifying the DAQ software for our system.

C. Gantry

The gantry and electronic housing is designed and under construction. We still need to design and build the septa and patient bed. Fig. 4 shows a photograph of the top and bottom aluminum arc plates with some of the CTI ECAT HR+ detector modules mounted in place. The detector

modules are individually positioned to point towards the center of the camera, as discussed in Section IIA.

Fig. 5 shows a 3-D drawing of the camera with many of the gantry and electronic housing details. The upper bank is mounted onto a main aluminum back-plate in order to control the vertical motion using a hand-crank, allowing upward movement for patient access and downward to maximize sensitivity. A second hand-crank is used to adjust the overall tilt of both upper and lower banks. The near end of Fig. 5 also shows the electronic housing. The six DHI boards are mounted horizontally to the housing that holds their corresponding Analog Subsection boards. The Coincidence Processor board is mounted onto the cabinet door for compactness. The ±5V and high voltage power supplies are mounted on the far end.

III. Expected Performance

A. Point Source Grid

To determine the size of the region of high spatial resolution, we have performed statistical noise-free simulations. Fig. 6 shows reconstructed point sources in a grid. Data are generated with interactions throughout the crystal, assuming an attenuation length of 10 mm in the BGO crystal. A preliminary iterative maximum likelihood algorithm is used in the reconstruction without correcting for detector penetration. The point sources are 5 cm apart, and the grid covers the majority of the field of view. All point sources are clearly visible in the image (black = high uptake). As expected, increased radial blurring due to penetration effects is seen in the region representing the outer edge of the patient. Since we are optimizing resolution at the center near the prostate at the price of resolution at the edges, distant metastases will suffer from some resolution degradation. However, good resolution is observed in the 10 cm diameter central region near the prostate. In Fig. 6, the central point has both a radial and tangential fwhm of 2 mm. More representative of the expected spatial resolution, the surrounding eight points have a radial fwhm of 4 mm and tangential fwhm of 3 mm. Improved resolution for more distant points is expected when the reconstruction corrects for detector penetration, although this process increases the statistical noise in the reconstruction.

Assuming that the detector arcs are rigid with a fixed focal spot for each arc, both focal spots are at the center for the 'nominal' gap separation. The above simulation (Fig. 6) assumed this 'nominal' gap distance. In order to investigate the effect of varying the gap between the arcs, the simulation is repeated for a gap range of ±5 cm when the focal spots are no longer in the center. The same minimal blurring within a 10 cm diameter central region is observed for both cases, indicating that a wide range in patient size will not compromise the resolution near the prostate. Fig. 7 shows the reconstructed point source grid with the gap distance increased by +5 cm from 'nominal' position.

The above results show that we can achieve similar resolution in the 10 cm diameter center region as an ECAT HR+ scanner. Using the nominal configuration, we also compute the signal to noise ratio (SNR) of an ideal observer for detecting a small lesion at the grid locations. The background is modeled as an uniform elliptical region (major axis = 40 cm, minor = 30 cm). For the central point, the resulting SNR of the new system is about 27% higher than that of an ECAT HR+ scanner under the same situation, and the SNR is about 20% higher for the surrounding eight points. This indicates that while the resolution is similar, the increase in sensitivity can still improve lesion detection. The above computation is for one 2D direct plane. No random or scattered events are modeled for either scanner.

B. Extended Sources

Monte Carlo methods are used to study the reconstruction of extended sources. Reconstructions are performed with an iterative maximum likelihood technique that assumes statistical noise representing 745 kcounts/slice, a tumor activity concentration that is two times the background activity concentration, 30% scatter fraction, and 20% randoms fraction. The reconstructions are then post-filtered with a very conservative Gaussian function of sigma = 1 pixel = 2 mm. We simulate self-attenuation by assuming a constant attenuation coefficient of 0.0095/mm inside the body. Coincidences between detector modules within the same bank and plane are allowed. Fig. 8(a) shows the body outline of a patient with an extended "prostate" source (2.5 cm diameter circle) with "tumors" in the upper right and lower left quadrants. Fig. 8(b) shows a reconstructed image of the phantom with "tumors" in the upper right and lower left quadrants clearly visible (white = high uptake), demonstrating that we can reconstruct nearly artifact-free images as well as detect and differentiate partial and whole prostate tumors. Our preliminary rate calculations indicate that 745 kcounts per imaging plane will be achievable with a six minute scan after a 10 mCi injection [16]. A relatively short value of six minutes is chosen to demonstrate that good images can be obtained even if the bladder fills rapidly. All published [^{11}C]choline or [^{18}F]fluorocholine studies done to date have used three minutes or longer (up to 30 minutes) imaging times.

C. Data Correction

Our design has sufficient room to incorporate a single photon or positron emitting source for transmission scans, but it would add to the camera cost. We plan to correct without an additional source using calculated attenuation coefficients based on body contours and an uniform attenuation coefficient [16]. Anatomical boundaries can be obtained from the outer edges of emission sinograms acquired from transverse sections [17]. It may also be possible to use heterogeneous attenuation coefficients by identifying tissue types (*e.g.*, soft tissue, bone, and air) based on x-ray CT images.

Because of the unusual geometry of our camera, the sensitivity of each line of response depends on the distance between the two detectors and the face angles of the two detectors; the shorter the distance is, the higher the

sensitivity. Normalization will include geometric correction (sensitivity changes caused by the septa that are not modeled in the solid angle computation), block effect correction, individual detector sensitivity correction, and dead time correction. These factors will be obtained using a scan of an uniform activity plane source such as used in conventional PET scanners. However, because of our specialized geometry and lack of rotational symmetry, the method for deriving the first two factors will be different from that of circular systems and may require a longer scan time to achieve good count statistics.

Random events will be estimated using the delayed window technique. Instead of pre-subtracting histogrammed data, delayed events will be saved in the list mode data stream with a tag to distinguish them from prompt events. For our statistical reconstruction algorithm, the estimated randoms will be included in the forward model in reconstruction.

IV. Discussion

This project is in its initial building phase, so there are many remaining uncertainties, including which radiopharmaceutical will be used, the specific requirements for the radiopharmaceutical and imaging procedure, and the accuracy that physicians would require to perform effective diagnosis and evaluate response to therapy. However, new PET radiopharmaceuticals have recently demonstrated promising results in the sensitive detection of prostate cancer. This PET camera design is also likely to out-perform whole body PET for this task, as the higher sensitivity will help for the short scans that appear to be necessary with choline-like radiopharmaceuticals.

Accurate patient positioning is also critical due to the limited (8 cm) axial extent of the camera. A manually placed external or trans-rectal positron-emitting source could be used to position the prostate near the center of the FOV of the camera. Alternatively, the prostate is visible in ultrasound images acquired with an external transducer, and these images could be used to position the patient bed.

Finally, as Fig. 1 shows, it is difficult to identify features other than the prostate (and possibly the bladder) in the PET images. Local anatomic information is highly desirable to determine the location of the disease within the prostate, as well as to determine whether the disease has spread to the prostate bed. This information could be obtained with dual modality imaging. X-ray CT provides excellent images of the abdomen, but the cost is relatively high. Ultrasound imaging with a trans-rectal probe provides reasonable detail in the region of the prostate and the cost of an ultrasound unit is significantly less than that of a CT imager, so we plan to explore adding co-registered ultrasound imaging capability.

V. Conclusion

Promising new PET tracers for prostate cancer, such as [^{11}C]choline and [^{18}F]fluorocholine, have motivated us to design and build a low cost PET camera optimized for prostate imaging. Monte Carlo simulations demonstrate the feasibility of detecting and differentiating partial and whole prostate tumors with a tumor to background ratio of 2:1, using a six minute scan after a 10 mCi injection. Simulations also predict minimal blurring in the 10 cm diameter central region for a wide range in patient size. Thus, we are currently building a camera that will image prostate tumors with good spatial resolution and image contrast at low cost relative to commercial PET scanners.

VI. Acknowledgment

We thank Dr. Hara from the International Medical Center of Japan for providing the PET images presented in Fig. 1 of this paper. We also thank Dr. Nutt from CPS Innovations for providing detectors and electronics. This work was supported in part by the Director, Office of Science, Office of Biological and Environmental Research, Medical Science Division of the U.S. Department of Energy under Contract No. DE-AC03-76SF00098 and in part by Department of Defense grant number DAMD17-02-1-0081. Reference to a company or product name does not imply approval or recommendation by the University of California or the U.S. Department of Energy to the exclusion of others that may be suitable.

VII. References

1. H. I. Scher and L. W. Chung, "Bone metastases: improving the therapeutic index," *Semin Oncol*, vol. 21, pp. 630-56, 1994.
2. H. I. Scher, M. Mazumdar, and W. K. Kelly, "Clinical trials in relapsed prostate cancer: defining the target," *J Natl Cancer Inst*, vol. 88, pp. 1623-34, 1996.
3. M. A. Eisenberger and W. G. Nelson, "How much can we rely on the level of prostate-specific antigen as an end point for evaluation of clinical trials? A word of caution! [editorial; comment]," *J Natl Cancer Inst*, vol. 88, pp. 779-81, 1996.
4. J. Kurhanewicz, D. B. Vigneron, H. Hricak, et al., "Three-dimensional H-1 MR spectroscopic imaging of the in situ human prostate with high (0.24-0.7-cm3) spatial resolution," *Radiology*, vol. 198, pp. 795-805, 1996.
5. J. Kurhanewicz, D. B. Vigneron, R. G. Males, et al., "The Prostate: Magnetic Resonance Imaging and Spectroscopy: Present and Future," in *Radiologic Clinics of North America*, H. Hricak and P. R. Carroll, Eds. New York, New York: W. B. Saunders Co., 2000, pp. 115-138.
6. T. Hara, N. Kosaka, N. Shinoura, et al., "PET imaging of brain tumor with [methyl-C11]choline," *J Nucl Med*, vol. 38, pp. 842-7, 1997.
7. N. Shinoura, M. Nishijima, T. Hara, et al., "Brain tumors: detection with C-11 choline PET," *Radiology*, vol. 202, pp. 497-503, 1997.
8. T. Hara, N. Kosaka, and H. Kishi, "PET imaging of prostate cancer using carbon-11-choline," *J Nucl Med*, vol. 39, pp. 990-5, 1998.
9. T. Hara, N. Kosaka, T. Kondo, et al., "Imaging of brain tumor, lung cancer, esophagus cancer, colon cancer, prostate cancer, and bladder cancer with [C-11]choline," *J Nucl Med*, vol. 38 (suppl), pp. 250P (abstract), 1997.
10. T. Hara, K. Inagaki, N. Kosaka, et al., "Sensitive detection of mediastinal lymph node metastasis of lung cancer with 11C-choline PET," *J Nucl Med*, vol. 41, pp. 1507-13, 2000.
11. I. J. Jong, T. H. Que, J. Pruim, et al., "Imaging of bladder cancer using carbon-11 choline positron emission tomography," *J. Nucl. Med.*, vol. 41 (5 Suppl), pp. 74, 2000.
12. J. Kotzerke, J. U. Prang, B. Neumaier, et al., "Carbon-11 choline positron emission tomography (PET) of prostate cancer -- first clinical experience," *J. Nucl. Med.*, vol. 41 (5 Suppl), pp. 74, 2000.
13. J. Kotzerke, J. Prang, B. Neumaier, et al., "Experience with carbon-11 choline positron emission tomography in prostate carcinoma," *Eur J Nucl Med*, vol. 27, pp. 1415-9, 2000.
14. T. R. Degrado, R. E. Coleman, S. W. Baldwin, et al., "Fluorine-18-fluorocholine (FCH) as an oncological PET tracer: evaluation in

murine prostate cancer xenograft model," *J. Nucl. Med.*, vol. 41 (5 Suppl), pp. 231, 2000.

15. T. R. Degrado, R. E. Coleman, S. Wang, et al., "Synthesis and Evaluation of F18-labeled Choline as an Oncologic Tracer for Positron Emission Tomography: Initial Findings in Prostate Cancer," *Cancer Research*, vol. 61(1), pp. 110-117, 2001.
16. J. S. Huber, S. E. Derenzo, J. Qi, et al., "Conceptual Design of a Compact Positron Tomograph for Prostate Imaging," *IEEE Trans Nucl Sci*, vol. NS-48, pp. 1506-1511, 2001.
17. T. F. Budinger and G. T. Gullberg, "Three-dimensional reconstruction in nuclear medicine emission imaging," *IEEE Trans Nucl Sci*, vol. NS-21, pp. 2-20, 1974.

Figures:

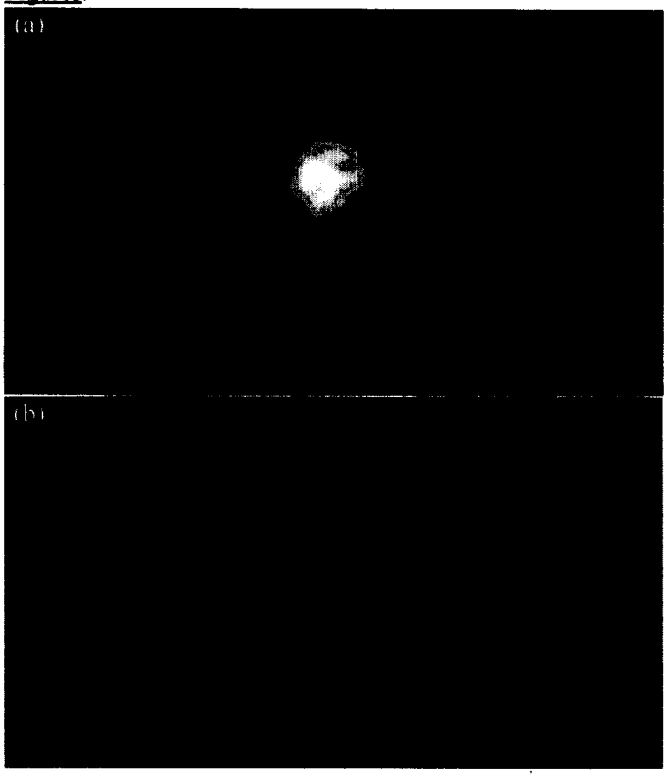

Fig. 1: [^{11}C]choline image of prostate cancer (a) before and (b) after treatment. These grayscale images indicate a high (white) uptake in the prostate cancer compared with a low (gray) uptake elsewhere. Images are provided by Hara and co-workers [8].

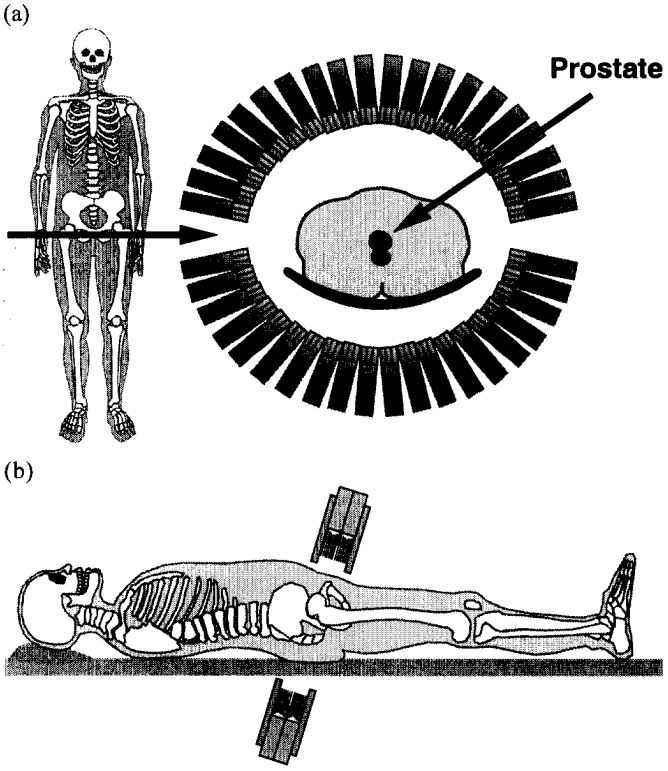

Fig. 2: Positron tomograph for prostate imaging. (a) Drawing of a transaxial view through prostate, showing the patient centered between two detector banks. The individual detector modules are angled to point towards the prostate. (b) Drawing of the sagittal view. The bottom arc is fixed below the patient bed, whereas the top arc adjusts vertically for patient access and compactness. Both detector banks are tilted and positioned as close as possible to the prostate, which improves sensitivity and minimizes attenuation.

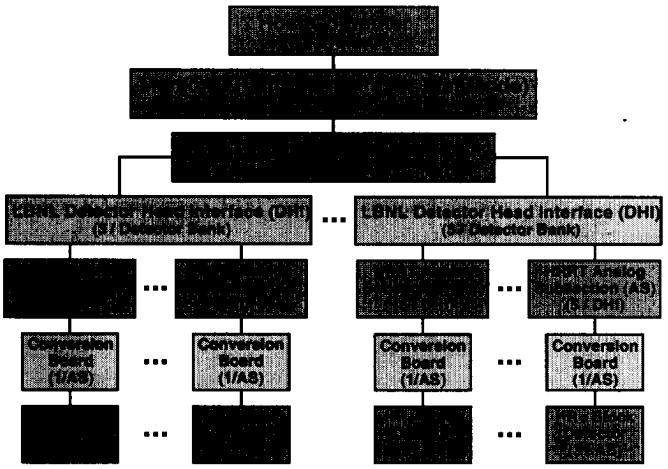

Fig. 3: Diagram of the complete data collection chain, showing the custom LBNL and CTI components and their inter-relations. The camera will use 80 CTI ECAT HR+ block detectors, 28 LBNL conversion boards, 28 CTI HRRT Analog Subsection boards, 6 LBNL custom Detector Head Interface boards, 1 CTI Coincidence Processor and a PC.

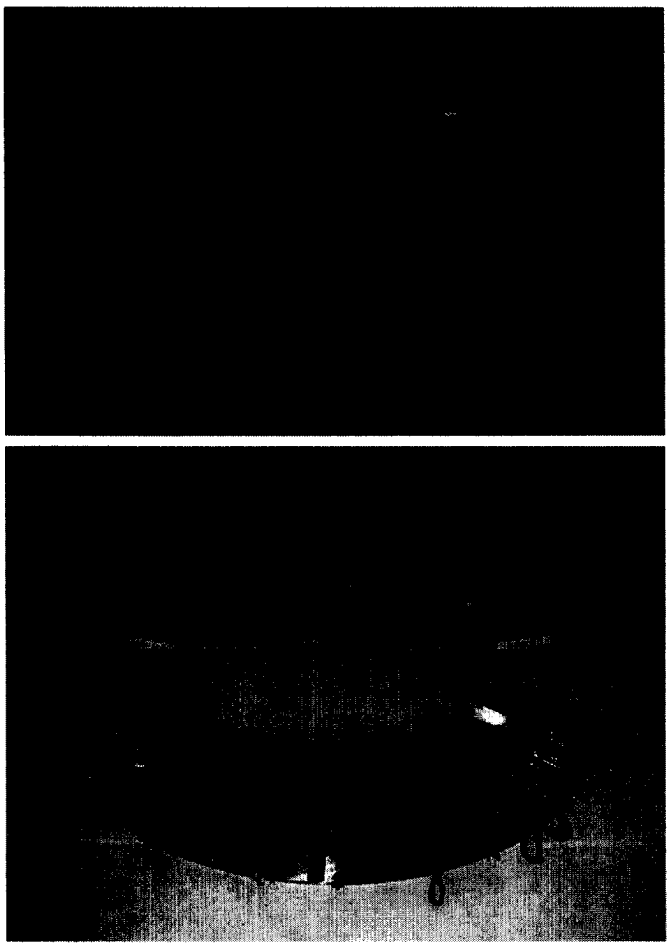

Fig. 4: (a) CTI ECAT HR+ detector module with an aluminum guide epoxied along its midline. (b) Photograph of the top and bottom aluminum arc plates with some of the CTI ECAT HR+ detector modules mounted in place. Each detector module has an aluminum guide that slides along a groove in the arc plate and is stopped (and secured against the arc plate) using a mortise and tenon. The detector modules are individually angled to point towards the center of the camera.

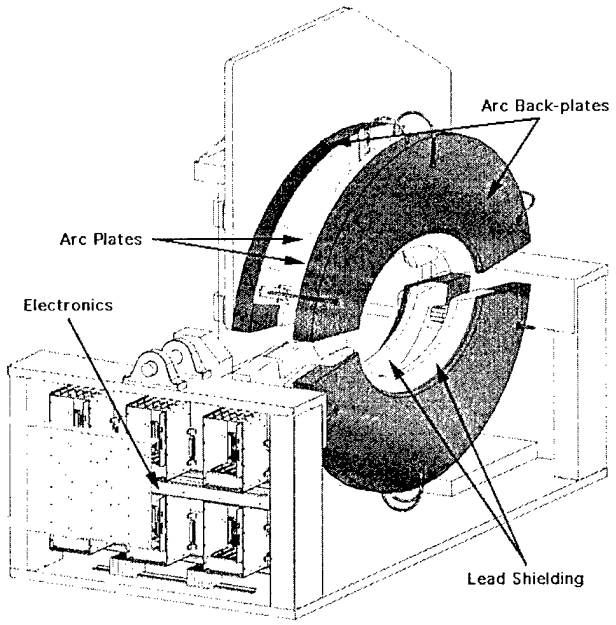

Fig. 5 3-D drawing of the prostate PET camera with some gantry details, as viewed from the side. Only a few detector modules are shown in place. The arc plates (with detector module grooves, shown in Fig. 4b) are mounted onto thicker aluminum arc back-plates that also hold the lead shielding in place. The arc plates (white), arc back-plates (dark gray) and lead shielding (light gray) are symmetric (~left and right in drawing) since there are two axial rows of detector modules. The upper bank is mounted onto a main aluminum back-plate in order to control the vertical motion using a hand-crank, allowing upward movement for patient access and downward to maximize sensitivity. A second hand-crank is used to adjust the overall tilt of both upper and lower banks. The near end of the drawing shows the electronics. The six DHI boards are mounted horizontally to the housings that hold their corresponding Analog Subsection boards. The Coincidence Processor board is mounted onto the cabinet door. The power supplies are mounted on the far end of the gantry. Most of the cabling is not shown, as well as the patient bed.

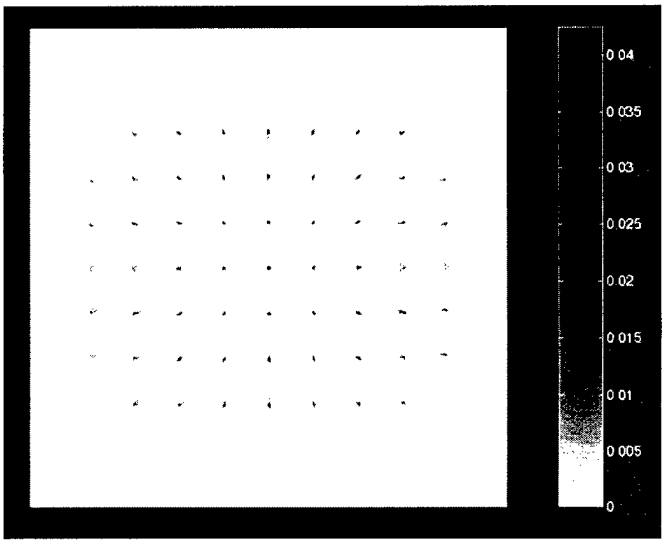

Fig. 6: Statistical noise-free reconstructed image of a point source grid when arcs are separated by the 'nominal' distance. The point sources are 5 cm apart, with the grid covering the majority of the field of view. Most point sources are located between pixels (*i.e.*, the center point source contributes to four nearby pixels). All point sources are visible (black = high uptake). Increased radial blurring is observed near the outer surface of the patient as expected due to penetration effects. However, good resolution is demonstrated in the center near the prostate, with minimal blurring in a 10 cm diameter central region. The central point has both a radial and tangential fwhm of 2 mm. The surrounding eight points have a radial fwhm of 4 mm and tangential fwhm of 3 mm. Improved resolution is expected when the reconstruction corrects for detector penetration.

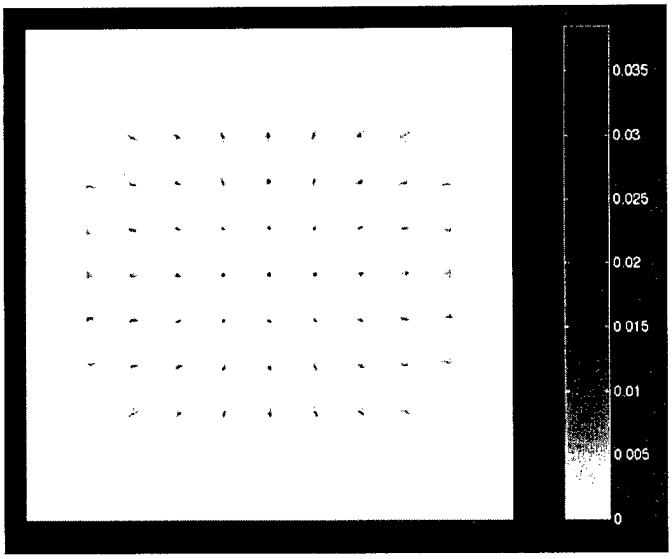

Fig. 7: Statistical noise-free reconstructed image of a point source grid when arc gap distance is increased by +5 cm from 'nominal' position. The point sources are 5 cm apart, with the grid covering the majority of the field of view. All point sources are clearly visible (black = high uptake). Good resolution is still demonstrated in the center near the prostate, with minimal blurring in a 10 cm diameter central region.

(a)

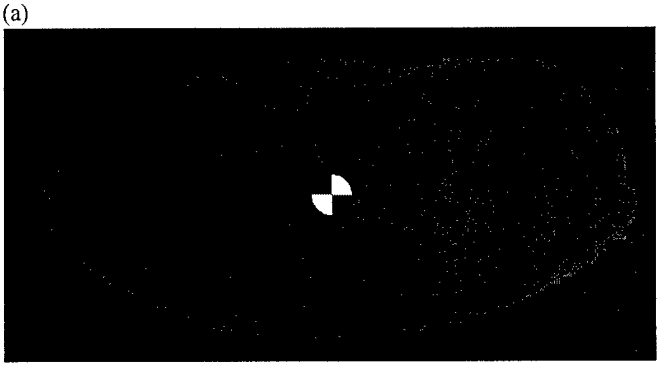

(b)

Fig. 8: (a) Body outline of patient with 2.5 cm diameter circular "prostate" divided into quadrants with "tumors" placed in the upper right and lower left quadrants (white = high uptake), assuming a tumor to background ratio of 2:1. The "patient" is 37.5 cm wide and 18.0 cm deep. (b) Reconstructed image of the phantom using an iterative maximum likelihood algorithm that assumes a 30% scatter fraction and 20% randoms fraction. Image represents 745 kcounts in a single slice, which should be achievable with a 6 minute scan after a 10 mCi injection. Both tumors are clearly visible.

Septa Design for a Prostate Specific PET Camera

Jinyi Qi, *Member, IEEE*, Jennifer S Huber, *Member, IEEE*, Ronald H Huesman, *Fellow, IEEE*, William W Moses, *Senior Member, IEEE*, Stephen E Derenzo, *Fellow, IEEE*, Thomas F Budinger *Member, IEEE*,

Abstract— **The recent development of new prostate tracers has motivated us to build a low cost PET camera optimized to image the prostate. Coincidence imaging of positron emitters is achieved using a pair of curved detector banks. The bottom bank is fixed below the patient bed, and the top bank, which is above the patient, moves upward for patient access and downward for maximum sensitivity. In this paper, we study the design of septa for the prostate camera using Monte Carlo simulations. The system performance is measured by the detectability of a prostate tumor and the conventional noise equivalent count (NEC). We have studied 27 septa configurations. The results show that the septa design has a large impact on the lesion detection at a given activity concentration. At the background activity level of 0.1 μCi/cc, sparse septa with 8-crystal spacing outperforms the traditional two-dimension (interplane septa) and three-dimension (septaless) designs in terms of both the lesion detection and NEC. Significant differences are also observed between the lesion detectability and NEC performance, indicating that the NEC does not correlate well with this lesion detection task.**

I. Introduction

Prostate cancer has a prevalence and diagnostic rate similar to breast cancer, with 360,000 new cases diagnosed each year and two million men affected by the disease in the United States. Prostate cancer suspicion is typically based on an elevated prostate-specific antigen (PSA) level or a suspicious node found during a digital rectal exam. Serum PSA values do not always correlate well with clinical diagnosis or outcomes. Palpation is subjective, insensitive and inexact. A new imaging technology for sensitive detection of early stage prostate cancer is needed to confirm initial diagnosis and help guide treatment decisions.

The recent development of new prostate tracers has shown promising results in detecting prostate cancer using carbon-11-choline [1]. This has motivated us to build a low cost PET camera optimized to image the prostate [2]. Coincidence imaging of positron emitters is achieved using a pair of curved detector banks. Fig. 1 shows the transaxial view of the camera. The bottom bank is fixed below the patient bed, and the top bank moves upward for patient access and downward for maximum sensitivity. Each bank consists of two axial rows of 20 block detectors (8×8 arrays of 4.5×4.5×30mm^3 BGO crystals), forming two arcs with a minor axis of 45 cm and major axis of 70 cm. Our prostate camera has about one-fourth the number of detectors as in a conventional PET system because: (a) the patient is not fully encircled in 2D, (b) the patient port is smaller, and (c) the axial coverage is only 8 cm. However, since the average distance to the detectors is approximately one-half that of a conventional 2D PET system, the solid angle for a central source is approximately double for average-sized men. Thus, we expect to achieve improved detection efficiency at a lower cost.

This work is supported in part by Department of Defense grant number DAMD17-02-1-0081, by the Director, Office of Science, Office of Biological and Environmental Research, Medical Science Division of the U.S. Department of Energy under Contract No. DE-AC03-76SF00098, and by National Institutes of Health grant number R01 EB00194.

The authors are with the Department of Nuclear Medicine and Functional Imaging, Lawrence Berkeley National Laboratory, Berkeley, CA 94720, USA.

Individual detector modules are angled to point towards the camera center near the prostate location in order to reduce penetration effects (in the detector) for annihilation photons originating in the prostate. This maintains high resolution selectively in the region of the prostate and is an unique feature of this non-circular camera geometry. Annihilation photons from other parts of the field of view (FOV) will suffer increased penetration effects, but these regions are less important. Both detector banks can be tilted to image the prostate while minimizing attenuation (i.e., above the buttocks and below the stomach), but the gantry allows zero tilt for thin patients. Despite this special geometry, we are able to reconstruct nearly artifact free images around the prostate region by using an iterative reconstruction algorithm [2].

The camera design includes septa to reduce background events from random coincidences and from Compton scatter photons in the patient. Here we study the effect of different septa designs on the system performance using Monte Carlo simulations. Septa designs have been studied for conventional PET scanners [3], [4], [5], [6], [7], [8], as well as the coincidence gamma cameras [9], [10], [11]. In this work we focus on the specific application and special geometry of the prostate camera. To better assess the image quality, we measure the detectability of a prostate lesion using an ideal linear observer, in addition to the noise equivalent count (NEC) that was primarily used in previous studies. We demonstrate the limitation of NEC for evaluating the prostate camera design.

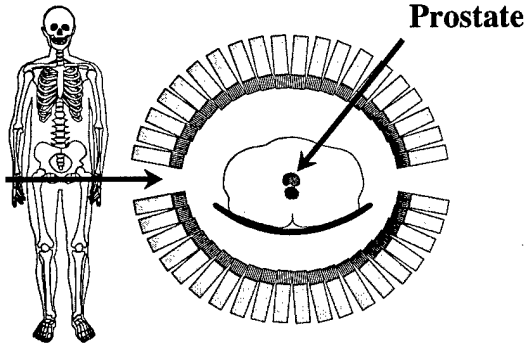

Fig. 1. A positron tomograph for prostate imaging [1].

II. Figures of Merit

A very popular figure of merit used to evaluate PET scanner design is the noise equivalent count, which is defined as

$$\text{NEC} = \frac{T^2}{T + S + kR} \tag{1}$$

where T, S, and R are total number of true coincidences, scattered events, and random events, respectively. Here we use $k = 1$ assuming the randoms are not pre-subtracted and the expectation of the randoms can be estimated separately. NEC represents the overall signal-to-noise ratio (SNR) of the data set and is not specific to any local region.

Since our camera is designed specifically for imaging prostate tumors, we believe that it is more appropriate to measure system performance for this particular detection task. We choose a "signal-known-exactly, background-known-exactly" (SKEBKE) task because the location of the prostate is relatively fixed and the background uptake is fairly uniform [1]. We use a prewhitening (PW) numerical observer, which is the ideal observer under Gaussian noise, to evaluate the lesion detectability. The performance of the PW observer measures the information content in the data for lesion detection.

Let $\boldsymbol{h}_1$ and $\boldsymbol{h}_0$ denote the expectations of the measurements with and without a lesion, respectively. The PW observer computes the following test statistic η for a given data set $\boldsymbol{y}$

$$\eta(\boldsymbol{y}) = [\boldsymbol{h}_1 - \boldsymbol{h}_0]' \, \boldsymbol{\Sigma}^{-1} \boldsymbol{y}, \tag{2}$$

where $\boldsymbol{\Sigma}$ is the ensemble covariance matrix of $\boldsymbol{y}$. A decision whether there is a lesion or not is then made by comparing this statistic to a pre-selected threshold. The detectability of the lesion can be measured by the SNR of $\eta(\boldsymbol{y})$, which is defined as

$$\text{SNR}^2 = \frac{[\eta(\boldsymbol{h}_1) - \eta(\boldsymbol{h}_0)]^2}{\text{var}[\eta(\boldsymbol{y})]}. \tag{3}$$

PET data can be modeled as independent Poisson random variables with the expectation $\bar{\boldsymbol{y}}$ related to the tracer distribution $\boldsymbol{x}$ through an affine transform

$$\bar{\boldsymbol{y}} = \boldsymbol{P}\boldsymbol{x} + \boldsymbol{s} + \boldsymbol{r},$$

where $\boldsymbol{P}$ is the projection probability matrix with the (i,j)th element denoting the probability of detecting an event from the jth voxel by the ith LOR, $\boldsymbol{s}$ and $\boldsymbol{r}$ denote the expectation of the scattered and random events, respectively. Using this model, we can show that

$$\begin{aligned} \text{SNR}^2 &= \boldsymbol{f}'\boldsymbol{P}'\text{diag}\left[\frac{1}{\bar{y}_i}\right]\boldsymbol{P}\boldsymbol{f} \\ &= \sum_i \frac{[\boldsymbol{P}\boldsymbol{f}]_i^2}{[\boldsymbol{P}\boldsymbol{x} + \boldsymbol{s} + \boldsymbol{r}]_i} \end{aligned} \tag{4}$$

where $\boldsymbol{f}$ is the tracer uptake of a prostate lesion. We have shown in [12] that the SNR computed in (4) is the same as the SNR of a PW observer applied to images reconstructed using the maximum *a posteriori* (MAP) principle, but not using the filtered backprojection method. The form in (4) is somewhat similar to that of NEC in (1). The major difference is that the SNR focuses only on the LORs that intersect with the lesion and the signal in each LOR is individually weighted by its variance.

When $\eta(\boldsymbol{y})$ is normally distributed, the SNR is related to the area under the ROC curve by the error function [13]. Therefore, we use (4) to measure the lesion detectability.

III. Monte Carlo Simulation

We use Monte Carlo simulation to estimate the true coincidence rate, scatters and randoms under each septa configuration. The Monte Carlo simulation is conducted using the SimSET software[1]. Both Compton and photo-electric interactions are simulated in the patient body and septa. The patient body is modeled as an elliptical region with major and minor axes being 40 cm and 32 cm, respectively, which is the medium size of six randomly selected male persons in our department. It has uniform activity and the attenuation coefficient of water. The axial length of the body in the simulation is 60 cm, beyond which the activity has little contribution to the data.

The current version of SimSET is limited to circular ring PET scanners. To study the special geometry of the prostate camera, we model the septa as part of the attenuation object as shown in Fig. 2. The material of the septa is tungsten. The shape of the septa is modeled as the difference of two elliptical regions with major and minor axes of the inner one being 57 cm and 32 cm, respectively, and those of the outer one $(1 + \alpha)57$ cm and $(1 + \alpha)32$ cm, respectively, where α is a constant ranging from 0.04 to 0.64. We use longer septa near the detectors that are further away from the radial center to limit their singles rates. We also studied two septa designs with uniform length and found comparable results. The top and bottom axial planes contain perfect absorber to prevent photons from escaping from the axial openings so that the acceptance of a photon is completely determined by the septa. Therefore, we can use a ring detector surrounding the whole object and the resulting sensitivity is the same as that of the prostate camera. To reduce the effect of the noise in Monte Carlo results, we rebin the data into one transaxial sinogram when calculating the lesion detectability using (4). The thickness of the septa varies from 0.4 mm to 2.4 mm. The axial spacing between the septa varies from half a crystal (2.4 mm) to 16 crystals (77.6 mm). Table I summaries the septa designs that we simulated.

True coincidence events and scattered events are binned separately. For all the results presented in this paper we use an energy threshold of 355 keV, except where noted otherwise. The singles rates are estimated by running the simulation in SPECT mode with the same number of photons. Random events are estimated from the singles rates by

$$r_k = \tau \cdot \text{singles}(i) \cdot \text{singles}(j), \tag{5}$$

where singles(i) and singles(j) are the singles rates of the two detectors forming the kth LOR, and $\tau = 12ns$ is the coincidence timing window. All events are then corrected for deadtime as described in Section IV.

[1] Available at http://depts.washington.edu/simset/html/simset_main.html

TABLE I
PARAMETERS OF THE SIMULATED SEPTA DESIGNS

No.	Spacing (crystal)	thickness (mm)	α
1	0.5	0.4	0.08
2		0.4	0.16
3		0.6	0.08
4		0.8	0.08
5	1	0.4	0.16
6		0.4	0.32
7		0.8	0.08
8		0.8	0.16
9		0.8	0.32
10		1.2	0.08
11		1.2	0.16
12		1.6	0.08
13		1.6	0.16
14		2.4	0.04
15	2	0.8	0.16
16		1.2	0.16
17		1.6	0.16
18	4	0.8	0.32
19		1.2	0.16
20		1.2	0.32
21		1.6	0.32
22	8	1.6	0.64
23		2.4	0.16
24		2.4	0.32
25		2.4	0.64
26	16		0.32
27	(no septa)		0.64

IV. DEADTIME MODEL

The deadtime of the camera is modeled similar to that described in [14]. Two parts of the deadtime are considered, one from the processing of single events in each detector block and the other from the coincidence processing circuit.

For each detector, the live time can be modeled as

$$d_i = e^{-\tau_{block} N \cdot \overline{\text{singles}}(i)} \tag{6}$$

where N is the number of detectors per detector block, $\overline{\text{singles}}(i)$ is the average singles rate of the individual detectors within the block, and τ_{block} is the time constant of the detector block. The sensitivity of the kth LOR due to the detector block deadtime is then

$$n_k = d_i * d_j, \tag{7}$$

where i and j are the indices of the two detectors forming the kth LOR.

The system wide coincidence processing live time is

$$Coinc.\ Live = e^{-\tau_{sys} Coinc.Load} \tag{8}$$

where τ_{sys} is the time constant, and $Coinc.Load$ is the ideal count rate experienced by the coincidence processing circuit. It is calculated as

$$Coinc.Load = \sum_k (t_k + s_k + 2r_k) n_k, \tag{9}$$

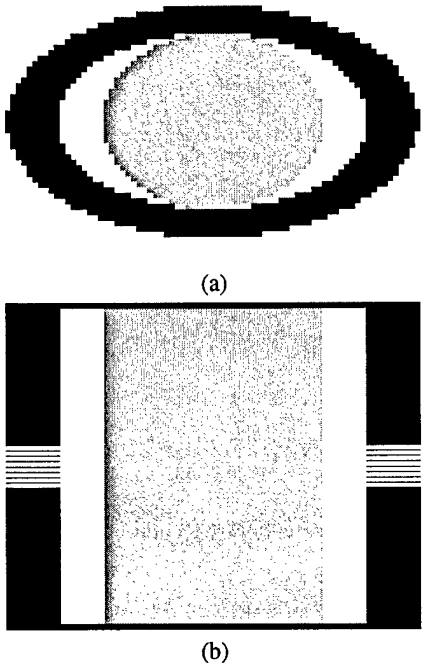

Fig. 2. Transaxial (a) and coronal (b) views through the center of the attenuation image used in the Monte Carlo simulation. The inner elliptical region is the patient body. The black band is the septa. The top and bottom axial planes contain perfect absorber to prevent photons from escaping from the axial openings. The parameters of septa shown in this figure are 2-crystal spacing, 1.2-mm thick, and $\alpha = 0.16$.

where t_k, s_k, and r_k are the ideal count rates of the trues, scatters, and randoms in the kth LOR, respectively. The factor of 2 accounts for the randoms in both prompt and delayed windows[2]. The overall sensitivity of the kth LOR due to the deadtime loss is $n_k * Coinc.Live$.

V. NORMALIZATION

A 20 cm diameter, 19 cm long uniform cylinder with activity concentration of 0.06 μCi/cc was scanned in an ECAT HR scanner (CTI PET systems, Knoxville, TN) in 3D mode. The measured singles rates are compared with that obtained from the Monte Carlo simulation of the same cylinder scan to calculate the detector efficiency. After scaling the simulation result with this calculated detector efficiency (=0.49), the true coincidence, scatters, and randoms are compared. Fig. 3 shows the measured and simulated projection profiles. The simulated scatter profile matches very well with the real measurement. The slight discrepancy between the measured and simulated true coincidence between 0 and -100 mm offset is due to the attenuation of the patient bed, which is not modeled in the simulation. The comparison between the randoms calculated from singles rates and that measured using delayed window shows a nearly perfect match (a ratio of 1.0). The simulated event rate of trues plus scatters also matches the measured event rate well (a ratio of 0.97). In addition to the detector efficiency, we also model the

[2]Here we assume that the events in the delayed window will be used to estimate the expectations of the random events.

missing data caused by the gap between the two detector banks (see Fig. 1) in the prostate camera simulations.

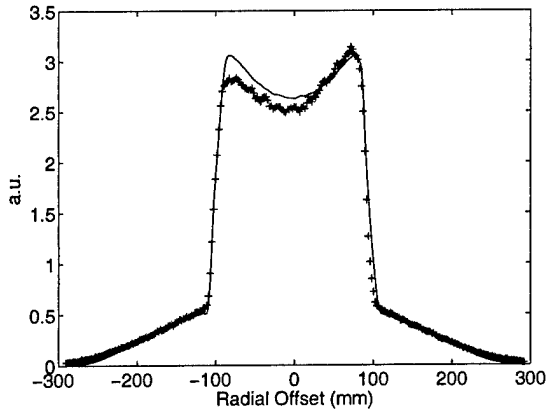

Fig. 3. Comparison between the measured ('+') and the simulated (solid line) projection profiles.

To estimate the time constants τ_{block} and τ_{sys} in the deadtime model, another uniform cylinder (the same geometry) with activity concentration of 0.6 μCi/cc was scanned in the ECAT HR scanner. The system deadtime as reported by the scanner is about 23%. The fitted time constants are $\tau_{block} = 2.2$ μs and $\tau_{sys} = 118$ ns.

VI. Results

A. Lesion detectability vs. NEC

We studied 27 different septa configurations (Table I). Fig. 4 shows the lesion detectability (SNR) and NEC of all the septa designs at different background activity levels. The simulated lesion is a 2.5-cm diameter sphere located at the center of the FOV. The lesion to background activity ratio is 2:1. The scan duration is 1 minute. Both lesion detectability and NEC show that longer and thicker septa are preferred for high activity concentration due to the reduction of scatters and randoms. However, doubling the length often has a stronger effect than doubling the thickness. The lesion detectability curves clearly show that sparse septa (more spacing) can improve lesion detection with the best peak SNR achieved by design no. 25 around 1.0-μCi/cc background activity level. In comparison, using sparse septa only increases the NEC at low activity levels, but not the peak NEC. Other significant differences are also observable between the SNR plots and NEC plots, indicating that NEC does not correlate well with this lesion detection task.

For the application of the prostate camera, we expect that the typical background activity concentration will be around 0.1 μCi/cc, which corresponds to a uniform uptake of 7.5-mCi injection into a 75-kg patient. In Fig. 5, we plot the SNR and NEC at 0.1 μCi/cc for all the septa designs. The results show that design no. 24 outperforms others in terms of both lesion detection and NEC, and so is the best septa configuration among all that we have studied.

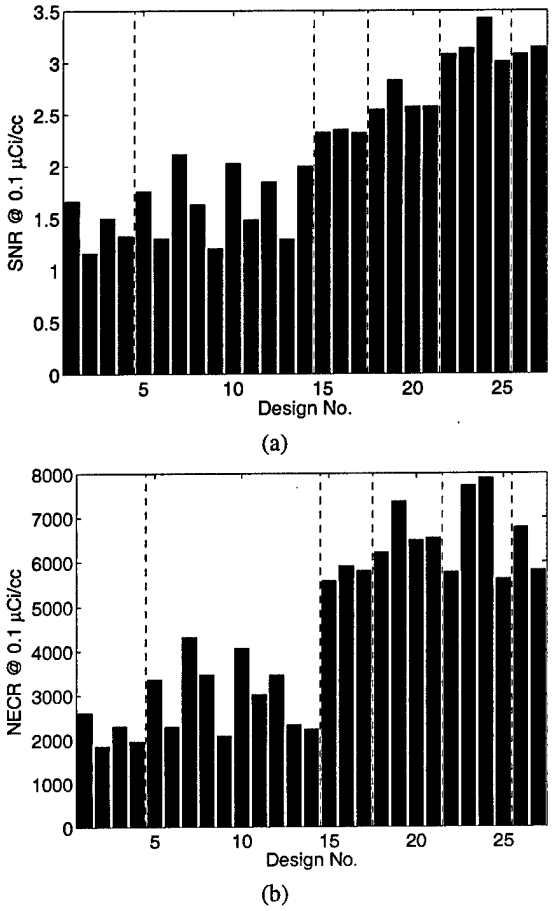

Fig. 5. Performance of all the septa designs at 0.1μCi/cc. (a) lesion detectability; (b) NEC. The design number refers to Table I. The dashed lines indicate the change in septa spacing.

B. Energy resolution

We studied the effect of energy resolution on septa design by varying the energy threshold in the Monte Carlo simulation. Fig. 6 shows the performance of a system with perfect energy resolution where we set the energy threshold to 511 keV, and Fig. 7 shows the performance of a system with poor energy resolution where the energy threshold is 200 keV. Comparing the two plots at the same activity level, we found that good energy resolution increases the lesion detectability and favors less septa due to the better rejection of events scattered inside the patient body and the septa.

VII. Conclusion

We have conducted Monte Carlo simulations to study the effect of septa configuration on lesion detection. The results clearly show that properly designed sparse septa can improve lesion detection over the traditional two-dimension (inter-plane septa) or three-dimension (septaless) configurations. Among all the designs that we studied here, we found that the septa with 8-crystal spacing give the best lesion detection and NEC at the background activity level of 0.1 μCi/cc. In future work we will

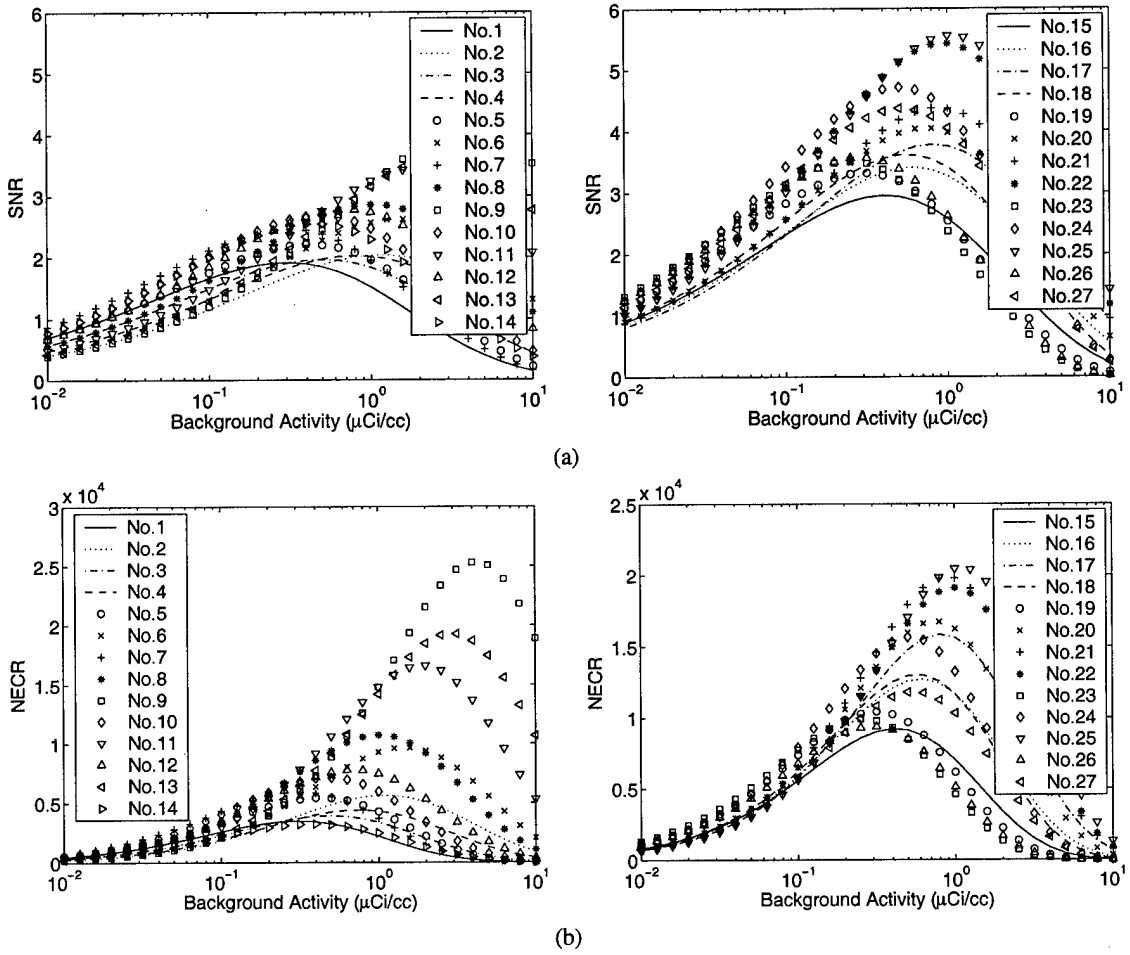

Fig. 4. Performance of 27 septa designs as a function of background activity levels. (a) lesion detectability plots; (b) NEC plots. The legend refers to the design number shown in Table I.

refine the search for the optimal septa design. We will also construct optimal septa designs and evaluate their performance using real measurements.

VIII. Acknowledgments

The authors would like to thank Robert Harrison at the University of Washington Medical Center, and Eric Frey and Ben Tsui at the Johns Hopkins University for their help in the SimSET software.

This work is supported in part by Department of Defense grant number DAMD17-02-1-0081, by the Director, Office of Science, Office of Biological and Environmental Research, Medical Science Division of the U.S. Department of Energy under Contract No. DE-AC03-76SF00098, and by National Institutes of Health grant number R01 EB00194.

References

[1] T. Hara, N. Kosaka, and H. Kishi, "PET imaging of prostate cancer using carbon-11-choline," *J. Nucl. Med.*, vol. 39, pp. 990–995, 1998.

[2] J. Huber, S. Derenzo, J. Qi, W. Moses, R. Huesman, and T. Budinger, "Conceptual design of a compact positron tomograph for prostate imaging," *IEEE Trans. Nucl. Sci.*, vol. 48, pp. 1506–1511, 2001.

[3] C. Thompson, "The effect of collimation on scatter fraction in multi-slice PET," *IEEE Trans. Nucl. Sci.*, vol. 35, pp. 598–602, 1988.

[4] L. E. Adam, J. S. Karp, and G. Brix, "Investigation of scattered radiotion in 3D whole-body positron emission using Monte Carlo simulations," *Phy. Med. Bio.*, vol. 44, pp. 2879–2895, 1999.

[5] R. Lecomte, "Analytical study of performance in a 3D PET scanner," *Phy. Med. Bio.*, vol. 37, pp. 623–634, 1992.

[6] M. Aykac, J. Uribe, H. Baghaei, H. Li, Y. Wang, Y. Liu, T. Xing, and W.-H. Wong, "Septa design study for volumetric imaging in positron emission tomography," *IEEE Trans. Nucl. Sci.*, vol. 49, pp. 2097–2102, 2002.

[7] T. Hasegawa, E. Tanaka, T. Yamashita, M. Watanabe, T. Yamaya, and H. Murayama, "A Monte Carlo simulation study on coarse septa for scatter correction in 3-D PET," *IEEE Trans. Nucl. Sci.*, vol. 49, pp. 2133–8, 2002.

[8] H. Baghaei, W. H. Wong, J. Uribe, H. Li, M. Aykac, Y. Wang, Y. Liu, T. Xing, and R. Farrell, "Brain lesion detectability studies witha high resolution PET operating in no-septa and partial septa configurations," *IEEE Trans. Nucl. Sci.*, vol. 50, pp. 1364–1369, 2003.

[9] C. J. Groiselle, Y. D'Asseler, J. A. Kolthammer, C. G. Matthews, and S. J. Glick, "A Monte Carlo simulation study to evaluate septal spacing using triple-head hybrid PET imaging," *IEEE Trans. Nucl. Sci.*, vol. 50, pp. 1339–46, 2003.

[10] T. C. Rust and D. J. Kadrmas, "Survey of parallel slat collimator designs for hybrid PET imaging," *Phy. Med. Bio.*, vol. 48, pp. N97–104, 2003.

[11] S. J. Glick, C. J. Groiselle, J. Kolthammer, and R. Z. Stodilka, "Optimization of septal spacing in hybrid PET using estimation task performance," *IEEE Trans. Nucl. Sci.*, vol. 49, pp. 2127–32, 2002.

[12] J. Qi and R. H. Huesman, "Theoretical study of lesion detectability of

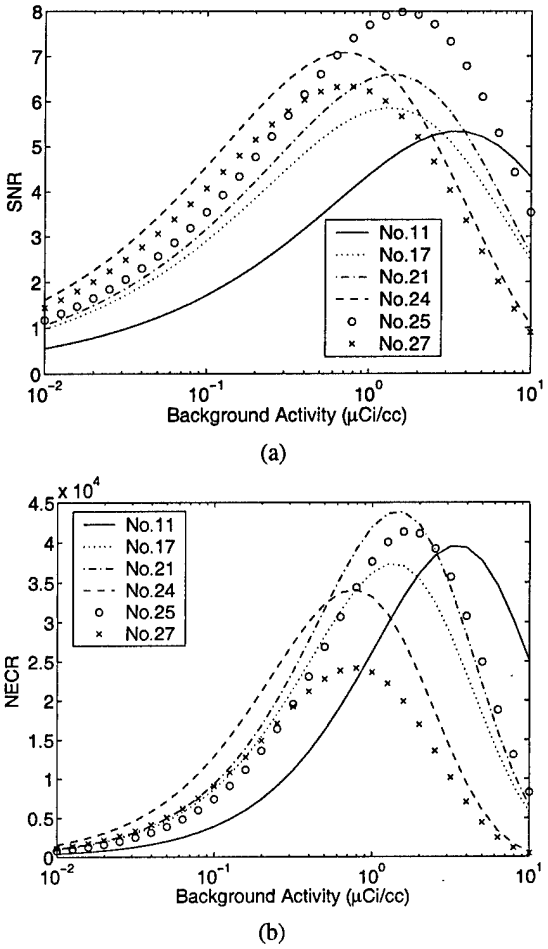

Fig. 6. Performance of a system with perfect energy resolution (energy threshold = 511 keV). (a) lesion detectability; (b) NEC. The design number refers to Table I.

MAP reconstruction using computer observers," *IEEE Trans Med Im*, vol. 20, pp. 815–822, 2001.

[13] H. H. Barrett, G. K. Abbey, and E. Clarkson, "Objective assessment of image quality. III. ROC metrics, ideal observers, and likelihood-generating functions," *Journal of Optical Society of America A*, vol. 15, pp. 1520–1525, 1998.

[14] L. Eriksson, K. Wienhard, and M. Dahlbom, "A simple data loss model for positron camera systems," *IEEE Trans. Nucl. Sci.*, vol. 41, pp. 1566–1570, 1994.

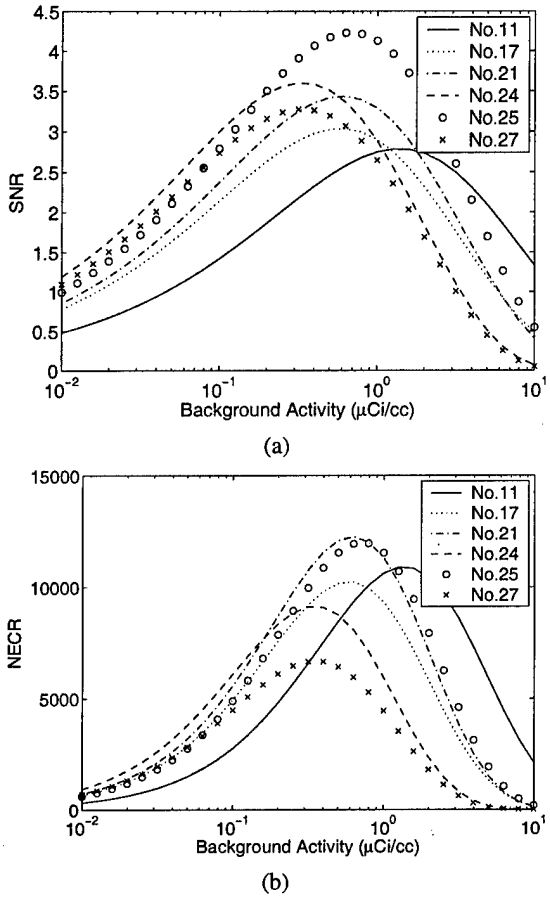

Fig. 7. Performance of a system with poor energy resolution (energy threshold = 200 keV). (a) lesion detectability; (b) NEC. The design number refers to Table I.